Parameter Development and Characterization of Laser Powder Directed Energy Deposition of Nb - Alloy C103 for Thin Wall Geometries

Colón, Brandon
Watanabe, Kurtis
Hobbs, Torren
Romnes, Carly
Mireles, Omar Roberto
Murr, Lawrence
Medina, Francisco

To be published in: Journal of Materials Research and Technology

DOI to publisher's version: 10.1016/j.jmrt.2024.04.200

Journal Pre-proof

Parameter Development and Characterization of Laser Powder Directed Energy Deposition of Nb – Alloy C103 for Thin Wall Geometries

Brandon J. Colón, Kurtis I. Watanabe, Toren Hobbs, Carly Romnes, Omar R. Mireles, Lawrence E. Murr, Francisco Medina

PII: S2238-7854(24)00974-8

DOI: https://doi.org/10.1016/j.jmrt.2024.04.200

Reference: JMRTEC 10606

To appear in: *Journal of Materials Research and Technology*

Received Date: 25 January 2024

Revised Date: 19 April 2024

Accepted Date: 22 April 2024

Please cite this article as: Colón BJ, Watanabe KI, Hobbs T, Romnes C, Mireles OR, Murr LE, Medina F, Parameter Development and Characterization of Laser Powder Directed Energy Deposition of Nb – Alloy C103 for Thin Wall Geometries, *Journal of Materials Research and Technology*, https://doi.org/10.1016/j.jmrt.2024.04.200.

Parameter Development and Characterization of Laser Powder Directed Energy Deposition of Nb – Alloy C103 for Thin Wall Geometries

Brandon J. Colón[a,b*], Kurtis I. Watanabe[a,b], Toren Hobbs[c], Carly Romnes[c], Omar R. Mireles[d], Lawrence E. Murr[b,e], Francisco Medina[a,b]

[a]Department of Aerospace and Mechanical Engineering, The University of Texas at El Paso, El Paso, Texas, USA
[b]W.M. Keck Center for 3D Innovation, El Paso, TX, USA
[c]NASA Marshall Space Flight Center, Huntsville, Alabama, USA
[d]Los Alamos National Laboratory, Los Alamos, New Mexico, USA
[e]Department of Metallurgical, Materials and Biomedical Engineering, The University of Texas at El Paso, El Paso, Texas, USA

[*]*Corresponding Author*

Abstract:
This work focuses on the parameter development and microstructural characterization of Nb-based alloy C103 for thin wall structures produced via laser powder – directed energy deposition (LP – DED). Laser power and scanning speeds were varied as part of a design of experiments to identify adequate print parameters. Combinations were evaluated for relative density, porosity, and geometrical accuracy. A combination of a laser power of 1420 W and scanning speed of 14 mm/s resulted in a relative density > 99%, exhibited a consistent weld bead profile and was used for further microstructural evaluation. A mix of optical and scanning electron microscopy (SEM) revealed small, slightly elongated grains along the edges and large epitaxial grains in the central region along the Build – Transverse view. Scanning electron microscopy (SEM) and energy dispersive spectroscopy (EDS) analysis revealed Hf rich columnar cells in the center that transition into an evenly spaced cellular structure towards the edges of the built sample. Electron backscatter diffraction (EBSD) scans show a sharp [001] texture when looking at the cross section of the sample along the build direction. The Build – Scan view revealed a zig – zag pattern that follows the back – and – forth deposition strategy that was used. Finally, microhardness measurements were taken in the as – built (AB) and stress relieved (SR) conditions to baseline preliminary mechanical properties. The AB condition exhibited a large amount of scatter in the data and averages up to 11% larger than the SR condition. The reduction in scatter upon applying the SR cycle are indicative of a large concertation of dislocations present in the AB condition.

Keywords:
- Additive Manufacturing
- Directed Energy Deposition
- Refractory Metals
- Thin Wall Structures
- Parameter Development

1 Introduction

The maturation and adoption of additive manufacturing (AM), also known as three – dimensional (3D) printing, has paved the way for increasingly complex designs that can be successfully manufactured. Coupled with developments in materials for high temperature applications, AM has

reduced lead times and increased performance of aerospace propulsion components such as propellant tanks, injectors, combustion chambers, and nozzles [1–9]. While many designs have leveraged the use of Laser Powder Bed Fusion (L – PBF), a variety of these components are simply too large for existing L – PBF platforms. Laser Powder – Directed Energy Deposition (LP – DED) can clear this hurdle, with commercial platforms offering build volumes from 0.6 m x 0.6 m x 0.6 m up to custom platforms of 7 m x 7 m x 36 m [10–17]. In this technology, powder is deposited through a set of nozzles which coalesces into a point that is being hit by a laser source, forming a melt pool and depositing material layer by layer as shown in Figure 1. Feature sizes on the order of 1 mm can be achieved with LP – DED by selecting an appropriate spot size and corresponding parameter set [18]. This allows for the creation of thin wall structures, in which a single bead is deposited throughout the profile of the printed component. This approach eliminates the need for a hatch and contour strategy, typical of L – PBF, and therefore reduces the number of variables during the parameter development process. It has been shown that thin wall structures exhibit different mechanical properties compared to bulk feature components (those with a hatch and contour strategy) [18,19] and therefore must be treated as a separate unique type of structure.

Material development for LP – DED has focused on steels, Al, Ti, Ni – based super alloys amongst others. While each of these have their unique set of advantages, many propulsion applications operate at temperatures in which these materials exhibit a significant drop in strength. Refractory metals offer a solution to this problem due to their ability to retain high strength at elevated temperatures and have relatively high melting temperatures (> 2000 °C).

Nb – based alloy C103 is one of the early refractory metals used in the aerospace community. It's ability to retain strength at elevated temperatures enabled its implementation in the nozzle extension of the Apollo Lunar Module [20]. It has a melt temperature of 2350 °C ± 50 °C, and contains approximately 10% Hf, 1% Ti and a mix of other elements shown in Table 1. The process to develop C103 components using traditional manufacturing methods, such as casting and forging, requires significantly long lead times. The high costs, buy-to-fly ratios from 20:1 to 50:1, and machining difficulty led to a decline in its use [21]. However, interest in this alloy has been renewed with the popularization of AM [22].

Table 1
Nominal composition of C103 per ASTM B655 [23].

	Nb	Hf	Ti	Zr	W	Ta
Wt. %	Bal.	9.0 – 11.0	0.7 – 1.2	< 0.7	< 0.5	< 0.5

Over the past decade, studies have focused on the development of pure Nb and C103 for AM technologies such as L – PBF and Electron Beam Powder Bed Fusion (EB – PBF) [21,22,24–29]. This summary of findings is based on bulk feature geometries that require a hatch and contour scanning strategy. Martinez et al. [24] successfully printed pure Nb components for the first time using EB – PBF. Their investigation of the microstructure found a columnar grain structure parallel to the build direction and hardness values ranging from 0.92 GPa to 1.1 GPa. Terrazas et al. [25] expanded on this work by characterizing the mechanical properties of pure Nb printed via EB – PBF. They were able to achieve relative densities over 99% and mechanical properties on the order of 140 MPa yield strength (YS) and 225 MPa ultimate tensile strength (UTS). Most recently, Liu et al. [26] studied pure Nb printed with L – PBF, achieving a relative density of 99.7%. In their study, the team showed the embrittlement effect due to increasing oxygen content during the build process and reported maximum YS of 550 MPa and UTS of 630 MPa.

Phillips et al. [22] manufactured spherical pre alloyed C103 powder from wrought ingot bars via electrode induction gas atomization (EIGA) for L – PBF and EB – PBF. Microstructures for both AM technologies showed elongated grains along the build direction. Tensile tests showed that the L – PBF parts in the as – built (AB) condition were substantially stronger than wrought materials at room temperature. At elevated temperatures, the printed samples had a lower yield strength (YS) while maintaining a higher ultimate tensile strength (UTS). At room temperature, EB – PBF components showed YS values close to wrought counterparts while the UTS was lower. At elevated temperatures the overall behavior was similar to wrought. Additional development for L – PBF was performed by Mireles et al [21]. Microstructural characterization revealed intra – granular HfO_2 precipitates as well as precipitates along the grain boundaries. The study evaluated mechanical properties for various heat treatments including Vacuum Stress Relief (SR) and Hot Isostatic Press (HIP). The printed parts were stronger than wrought across all heat treatments and testing conditions, further agreeing with the results by Phillips et. al [22].

Substantial work has been done by the community to advance LP – DED in general. Assessments of the field have been reported in great detail by DebRoy et. al [30], Dass and Moridi [31], and Svetlizky et. al [32] which serve as comparisons for this work. However, to the author's knowledge, at the time of writing there is no published data on the development of LP – DED C103, specifically for thin wall geometries. This lack of data can potentially hamper the adoption of C103 for LP – DED applications in many industries. The cost of C103 powder and the quantities needed for LP – DED can become considered a hurdle for its development. Common approaches to establish parameters based on trial – and – error or traditional statistical design of experiments (DOE) can require a high number of runs to identify an optimized parameter set. Therefore, it is imperative to show feasibility and to establish the corresponding printing parameters. This article presents the work done to address this issue by developing print parameters and characterizing the resulting microstructure of LP – DED C103 for thin wall geometries. These efforts will ultimately help promote its adoption by serving as a starting point for other users.

2 Methodology

A total of 14 specimens were 3D printed using pre alloyed gas atomized C103 powder with an RPM Innovation's 222 XR located at the W.M. Keck Center at the University of Texas at El Paso. A back – and – forth deposition strategy, shown in Figure 2, was used to build thin wall geometries with a target height of 25 mm. A 6.35mm thick Ti-6V-4Al plate was used as the substrate to build on. Each print was done in a recirculating argon inert environment such that the oxygen content was always below 10 ppm. These specimens were characterized for geometrical accuracy, density, and porosity. The effects of heat treatment on microstructure and hardness of the selected parameter set are explored and presented in the sections below.

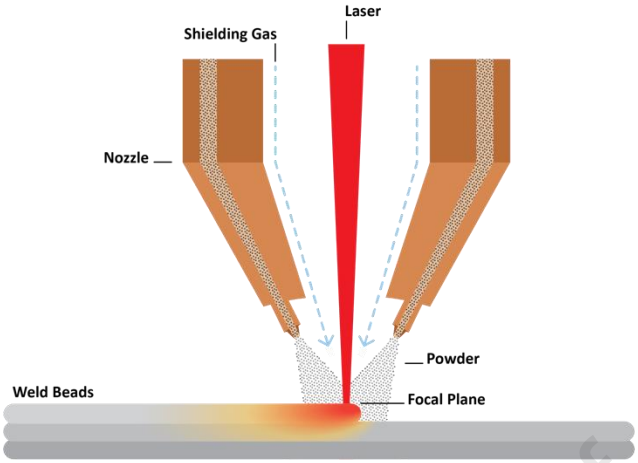

Fig. 1. Schematic of LP – DED deposition.

2.1 Design of Experiments

Due to the high cost of C103, the DOE was limited to two factors. Several studies have shown that laser power and scanning speed had the largest impact on melt pool dimensions in the LP-DED process [33–36]. A Latin Hyperspace Cube (LHS) sampling method was used to select the parameter sets to be tested. The LHS method is used to generate a quasi-random sample distribution and has been shown to be more effective at capturing nonlinearity effects compared to traditional fractional factorial designs [37,38]. In this method, the range of parameters is divided into partitions of equal probability [39]. To generate a parameter combination, laser power and scanning speeds are selected randomly from each space and paired. In this work, the author's made use of Python's open – source package SMT: Surrogate Modeling Toolbox to sample the design space [40]. The explored parameters are summarized in Table 2. Layer height and spot size were kept at constant values. Mass flow rate was selected to ensure slight overbuilding of the samples.

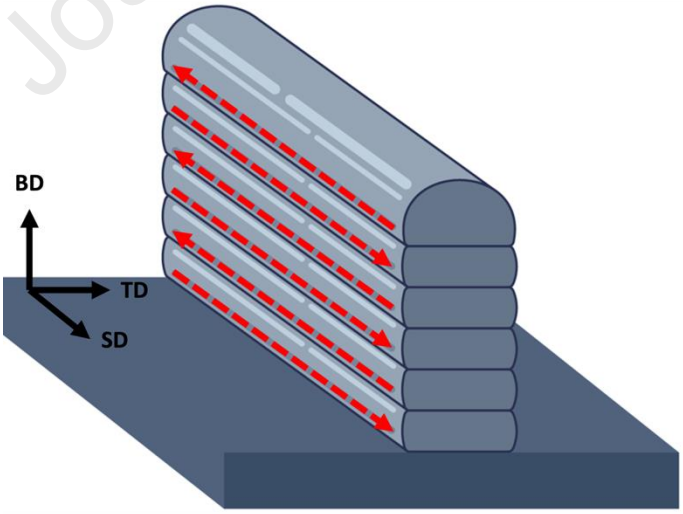

Fig. 2. Diagram of the build strategy used in this work. A back – and – forth scanning strategy, as indicated by the red arrows, was used to print specimens at a layer height of 2.5 mm. Directions are indicated as Build Direction (BD), Scanning Direction (SD), and Transverse Direction (TD).

Table 2

Laser Power and Scanning Speed combinations explored for the parameter development DOE.

Specimen #	1	2	3	4	5	6	7	8	9	10	11	12	13	14
Laser Power [W]	1050	788	1313	1050	1050	1341	1028	1420	951	1266	802	766	1142	608
Scanning Speed [mm/s]	12.70	12.70	12.70	9.50	15.80	11.00	9.73	13.96	13.12	14.81	8.88	11.43	12.27	10.16

2.2 Density & Porosity

Density measurements were done following the Archimedes principle per ASTM standard B311 – 22 and compared to the theoretical density of C103, 8.85 g/cm^3 [41]. Porosity was measured using a Keyence VHX-7000 microscope. Images were taken at 200x magnification and stitched together. The area fraction of porosity was then calculated using the microscope's built in Area Auto Measurement capability.

2.3 Heat Treatment

The rapid heating and cooling rates in LP – DED induce high residual stresses in the part [42–45]. Stress Relief (SR) heat treatments are commonly done for AM parts to minimize the risk of warpage during the build plate removal process. During the SR cycle, dislocations are redistributed, and no significant changes are expected to occur in the microstructure [46]. The SR cycle must be performed in a clean vacuum environment to prevent oxidation due to the oxygen sensitive nature of Nb alloys. The build was wrapped in tantalum (Ta) sheets as an added layer of protection against oxidation during the heat treatment cycle. Based on the work by Mireles et. al [21], a vacuum stress relief heat treatment was performed at 1100°C and held for 1 hour while the specimens were still attached to the build plate.

2.4 Metallographic Sample Preparation

The samples were hot mounted using Bakelite thermosetting powder and epoxy in a 1:2 ratio. The plane grinding was done using MD Piano pads at 220, 500 and 1200 grit size each for 3 minutes at a force of 25 N. Polishing was done using an MD Allegro pad with 9um diamond suspension for 10 minutes at 25 N, followed by an MD Chem pad with 0.1 colloidal silica for 20 minutes at 15 N of force. Two methods were used for etching the samples. The first, referred to here as light etching, performed the final polishing step with a solution of 90% of the 0.1 colloidal silica and 10% of hydrogen peroxide at 30% strength. The second etchant used was a mixture of 45% deionized water, 45% nitric acid (HNO_3) and 10% hydrofluoric acid (HF).

2.5 Microstructure Characterization

The microstructure of the printed samples was characterized using a variety of microscopy techniques and equipment including optical microscopy, scanning electron microscope (SEM), energy dispersive X-ray spectroscopy (EDS), and electron backscatter diffraction (EBSD) analysis. A Keyence VHX-7000 was used to collect optical images in the polished and etched conditions. A JEOL JSM-IT200 scanning electron microscope (SEM) was used to image samples using Secondary Electron and Backscattered Electron modes. A voltage of 15.0 kV and a working distance range between 9.5 and 10.5mm were used. EBSD analysis was performed on an FEI QUANTA 600 F operating at 20keV and a 6.0 spot size equipped with an Oxford Instruments Symmetry S2 detector. Samples were mounted on a 70deg pre-tilted specimen holder with a varying working distance. EBSD results include crystallographic texture, grain area and grain count.

2.6 Microhardness Measurements

Vickers microhardness data was collected with an HV 0.1 on the Struers DuraScan and aligned with ISO standard 6507-1 [47]. Three series were taken along the build direction and five series were taken perpendicular to the build direction for each sample. The start location for each data series was such that the distance between the first indentation and the edge of the specimen was 3 times the mean diagonal length of the indentation. Measurements along the build direction were spaced apart by a distance equal to 9 times the mean diagonal length between the center of two adjacent indentations. Measurements perpendicular to the build direction were spaced apart by a distance equal to 6 times the mean diagonal length between the center of two adjacent indentations. The difference between the distance of adjacent indentations for each series type was to enable all data points to be collected during the same testing iteration, while still following standard's required minimum distance between indentations to be at least 3 times the mean diagonal length for hard materials. To analyze the data, indentations the same distance away from the specimen edge were averaged and plotted.

3 Results & Discussion

A total of 4 specimens were immediately deemed unacceptable based on a visual inspection where the build failed due to severe lack of fusion. Figure 3A shows the resulting thin wall structure 3D printed with parameter set 14 (608W and 10.16 mm/s) which led to drastic lack of fusion. Figure 3B on the other hand was printed with parameter set 8 (1420 W and 13.96 mm/s) and led to a successful print. The remaining 10 specimens were further inspected for geometrical measurements, density, microhardness, and microstructure as discussed in the following sections.

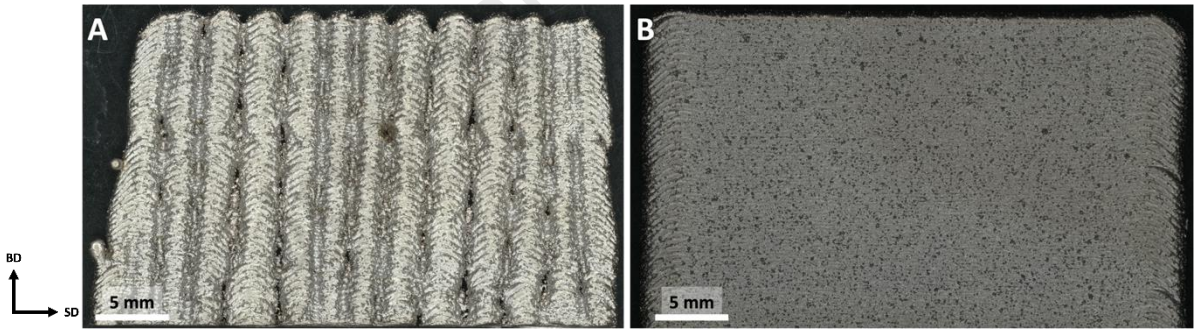

Fig. 3. Printed specimens from the parameter development DOE. (a) Drastic lack of fusion visible to the naked eye. (b) Successful print with a consistent geometry.

3.1 Powder Characterization

The size distribution of the powder plays a vital role in the outcome of AM builds, influencing layer height and flow rate during printing [48]. Highly spherical powders are preferred in LP – DED due to good flowability to reduce agglomeration in the delivery system [49]. For these reasons, the powder is inspected for its size distribution and shape. A Camsizer X2 was utilized to determine the powder size distribution (PSD) and its morphology. A total of three measurements were taken to ensure consistency; results show an average D10 of 64 μm, D50 of 82.1 μm, and D90 of 119.9 μm. Similarly, morphology results indicate high circularity as shown in the collected SEM images in Figure 4.

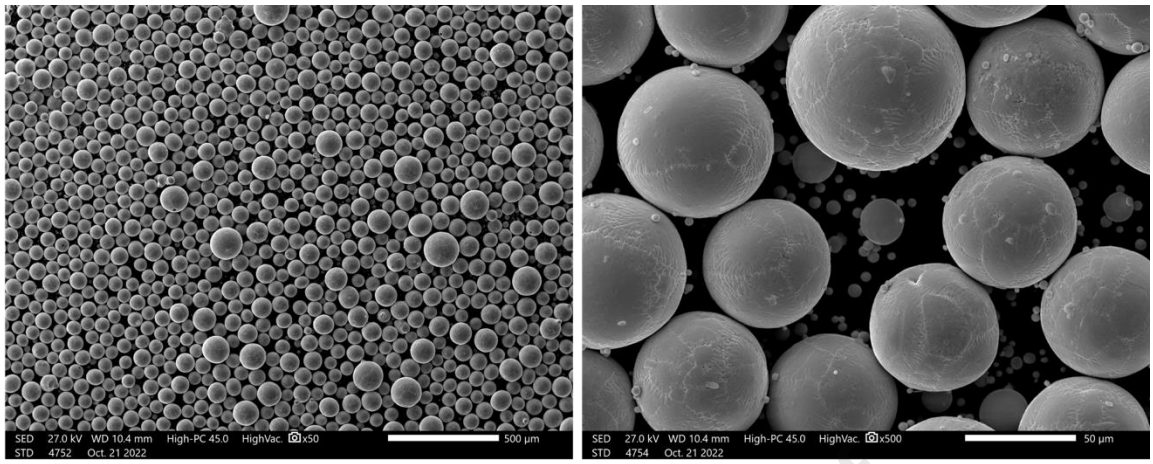

Fig. 4. SEM images of powder show highly spherical morphology across varying powder sizes**.**

3.2 Density & Porosity

A total of 11 specimens resulted in a relative density larger than 95%, with specimen 8 having the maximum relative density of 99.66%. Cross sections of the specimens were investigated for porosity, with all specimens reporting values less than or equal to 0.09%. No direct relationship was observed between the resulting relative density and porosity measurements. The observable evidence of porosity, such as that shown in Figure 5, was spherical in nature which is typically due to entrapped gas in the powder during the powder manufacturing process [50–52]. These results, summarized in Table 3, indicate that LP – DED can produce near fully dense C103 on par with other AM processes. For example, Mireles et. al [21] showed L – PBF components in the AB condition with a cross sectional porosity of 0.014%. Work by Philips et. al [22] using L – PBF resulted in low porosity of approximately 0.05%. EB – PBF C103 parts were near full density, however the authors did not provide numerical values [22].

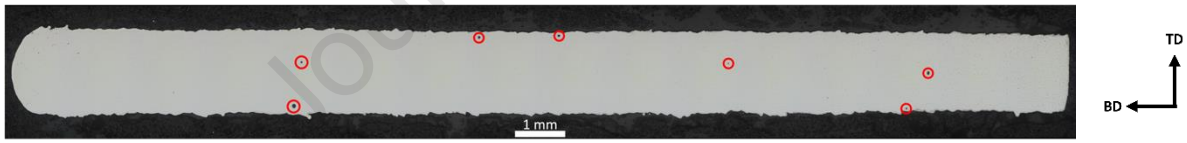

Fig. 5. Highlighted circular pores due to gas porosity in the BD – TD direction.

Table 3
Summary of density and porosity results for the measured specimens

Specimen #	1	3	4	6	7	8	9	10	11	13
Relative Density (%)	99.21	99.55	97.63	99.44	94.01	99.66	98.42	98.87	94.24	96.50
Cross Sectional Porosity (%)	0.040	0.050	0.090	0.004	0.074	0.021	0.036	0.075	0.052	0.061

3.3 Geometry

Several specimens can be considered fully dense due to having porosity values below 0.05% as shown in the previous section. While this may be considered as the target for successful parameter development in other AM technologies such as L – PBF and EB – PBF [22,50], it is not indicative of a parameter set that meets the geometrical accuracy required for a successful build in LP – DED. For example, parameter set #9 resulted in a porosity value of 0.036% while showing inconsistent thickness along the scanning

direction. Figure 6 shows a comparison between the specimens that exhibit drastic lack of fusion, inconsistent weld beads, and fully consistent weld beads.

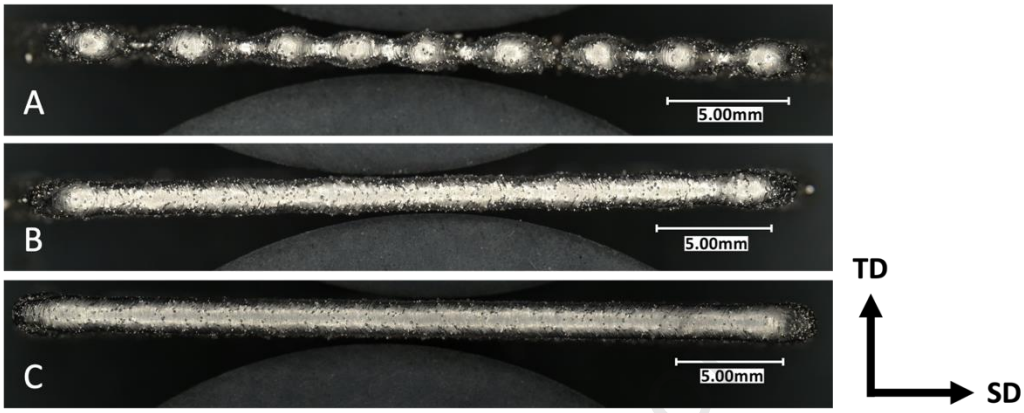

Fig. 6. Top view of DOE specimens. (a) Severe lack of fusion. Build Parameters: 608 W – 10.16 mm/s. (b) Inconsistent weld bead thickness. Build Parameters: 1050 W – 12.70 mm/s. (c) Consistent weld bead. Build Parameters: 1420 W – 13.96 mm/s.

Thickness values were measured with a caliper. However, due to the limitation in the accuracy, the reported values do not effectively capture the thickness variation along the weld bead. To address this issue, images were taken from the top with a Keyence VHX 7000. Using ImageJ, a total of 20 thickness measurements per sample were taken. Figure 7 shows the collected data for both measurement techniques, with specimen IDs corresponding to the parameter sets in Table 4. The average values are close together, with a maximum difference of 27% for sample 14. The standard deviation, plotted as error bars, serve as indication of the variation in thickness along the scanning direction. Specimens which exhibited drastic lack of fusion and inconsistent weld bead thickness had both larger error bars as well as larger differences between the digital and caliper-based measurements. On the other hand, specimens with consistent weld beads had a lower standard deviation and differences between digital and caliper measurements as low as 1.4%.

A total of three regions are identified as *Drastic Lack of Fusion*, *Inconsistent Weld Bead,* and *Consistent Weld Bead* as shown in Figure 8. The boundaries are based on linear regression fits through the parameter sets that comprise each region. Based on these, it is evident that specimens built with higher laser powers are more robust to changes in the scanning speed. Finally, the Pearson correlation coefficients were calculated for each of the DOE variables. This is a measure of the strength and directionality between the dependent and independent variable [53,54]. The coefficients for laser power and scanning speed were 0.854 and 0.072 respectively, indicating that laser power plays a larger role in controlling the weld bead thickness. These findings support the results of previous work by Feenstra et al. [33] where this relationship was established for a single scan. These results also demonstrate that the relationship is applicable and scalable to multilayer thin wall structures.

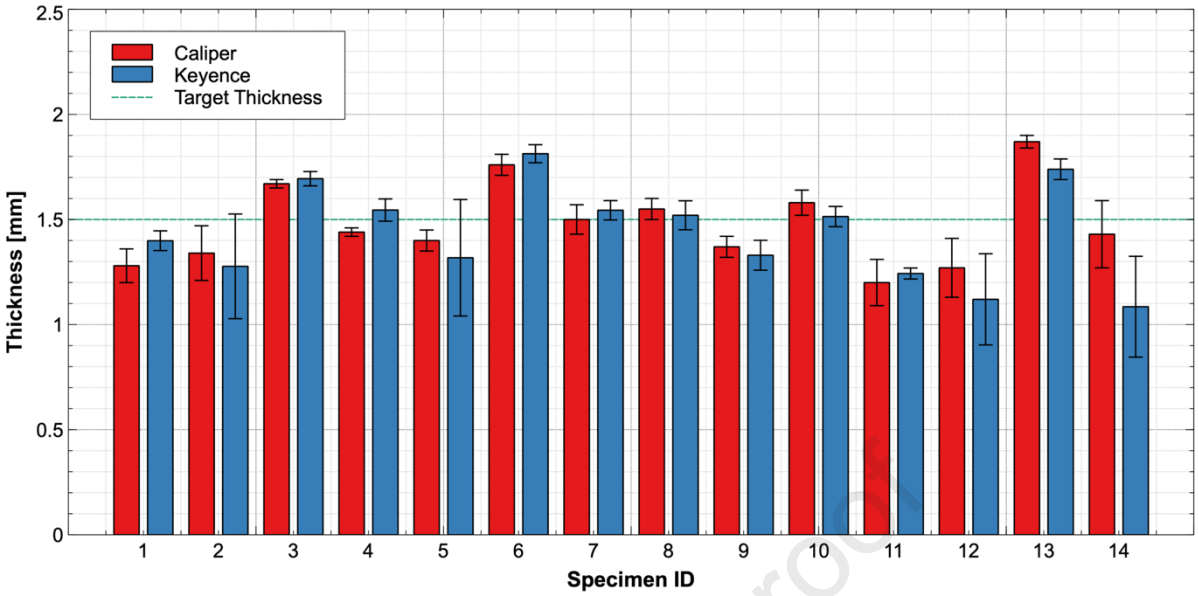

Fig. 7. Comparison of thickness measurements taken with a caliper and a Keyence VHX 7000 at x200 magnification.

Table 4
Summary of results for selected parameter set. Thickness measurements collected with Keyence VHX 7000.

Specimen #	1	2	3	4	5	6	7	8	9	10	11	12	13	14
Laser Power [W]	1050	788	1313	1050	1050	1341	1028	1420	951	1266	802	766	1142	608
Scanning Speed [mm/s]	12.70	12.70	12.70	9.50	15.80	11.00	9.73	13.96	13.12	14.81	8.88	11.43	12.27	10.16
Thickness [mm]	1.39 ± 0.04	1.27 ± 0.25	1.69 ± 0.03	1.54 ± 0.05	1.32 ± 0.27	1.81 ± 0.04	1.54 ± 0.05	1.52 ± 0.07	1.33 ± 0.07	1.51 ± 0.05	1.24 ± 0.03	1.12 ± 0.22	1.74 ± 0.05	1.08 ± 0.24

Based on these results, the authors recommend evaluating a geometrical feature of importance, in this case the weld bead profile, in addition to the relative densities when evaluating parameter sets for development efforts regarding LP – DED. Due to the high relative density, low porosity and consistent weld bead, parameter set #8 was selected for microstructural characterization and use for future builds. A summary of the results for this parameter set is presented in Table 5.

Table 5
Summary of results for selected parameter set.

Laser Power [W]	Scanning Speed [mm/s]	Relative Density %	Porosity %	Avg. Thickness [mm]
1420	14	99.66	0.021	1.55

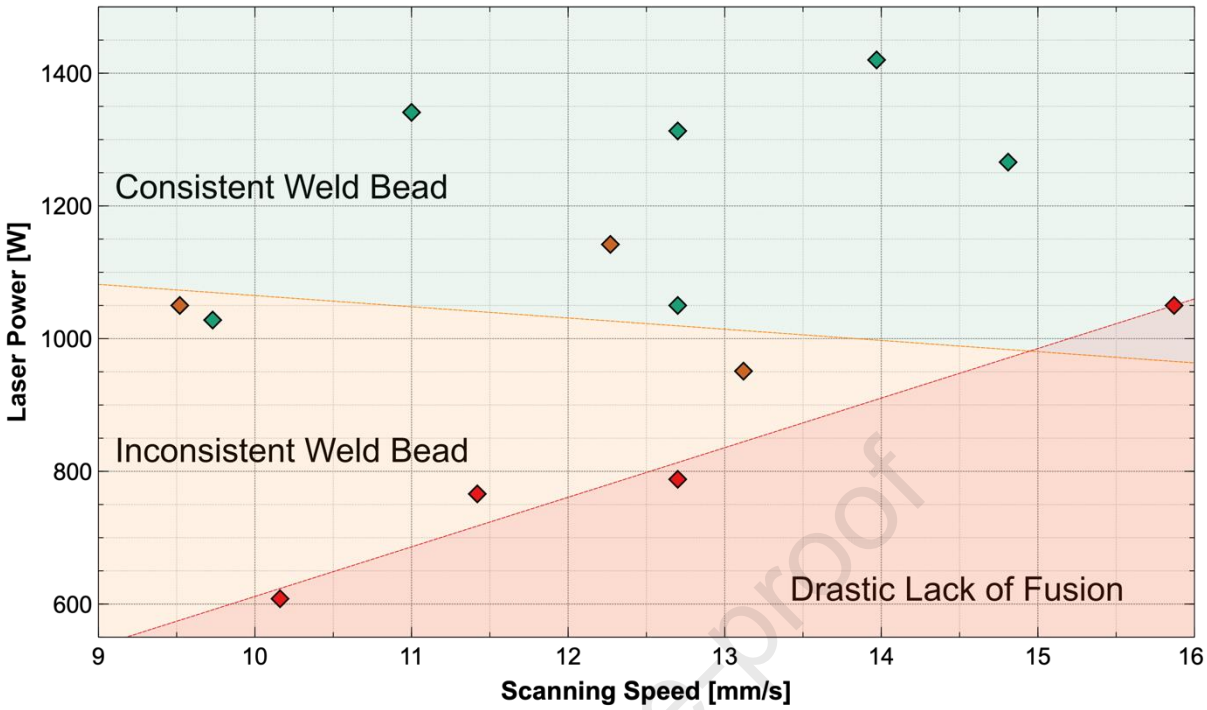

Fig. 8. Process parameter map with regions based on weld bead profile along the scanning direction.

3.4 Microstructure Characterization

Samples in the SR condition were sectioned and mounted for microstructural characterization. Micrographs in the as polished condition along the BD – TD direction are shown in Figure 9. Figure 9A slightly reveals grains along the edges and spherical porosity sporadically throughout, indicative of the high relative density achieved for this parameter set. At a higher magnification of x400, the layer of grains is approximately 250 μm to 300 μm deep as shown in Figure 9B. Additionally, instances of sintered powder are present along the edges, highlighted in Figure 9C. AM components are known to exhibit high surface roughness detrimental to the fatigue life [55–57]. In LP – DED, this behavior is due to the constant flow of powder during the 3D printing process. The incoming powder particles that are not captured by the melt pool can impact and adhere to the previously deposited layers. This has been recorded in work done by Gradl et. al [58] where they characterize the powder adherence for thin wall structures produced via LP – DED. Similarly, Gharbi et. al [59] provide an in depth discussion of this phenomena for LP – DED of Ti-6Al-4V. The low amount of sintered particles is indicative of a relatively low surface roughness, which makes it an attractive parameter set for components that will be subjected to fatigue environments. Further work is required to fully characterize the surface roughness and fatigue life of these components.

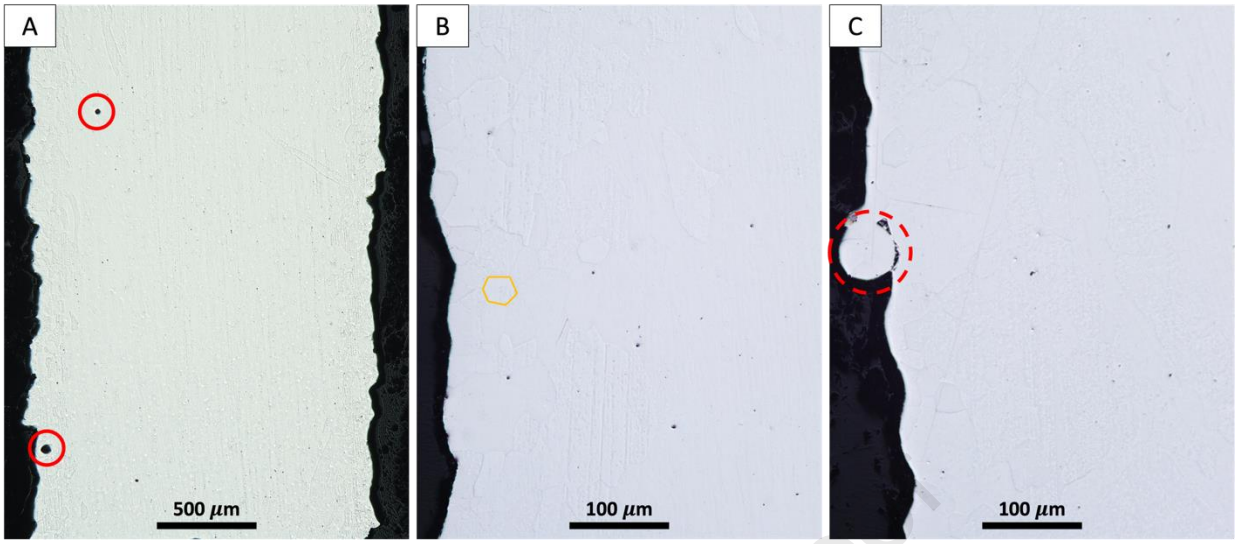

Fig. 9. Collection of micrographs in the as polished condition of the SR sample. (a) SR micrograph in the as polished condition along the BD – TD orientation at x80 magnification. Spherical porosity present sporadically throughout. (b) Region of small grains along the edges at x400 magnification. (c) Example of an adhered powder particle to the side of the printed thin wall structure at x400 magnification.

Upon etching the sample, sharp needle like structures and large grains in the center are revealed in Figure 10A. These structures in the central region appear to nucleate from the base of the 250 μm thick layers and are angled outwards in the direction of the edges of the part. The grains along the edges, now fully revealed, are slightly elongated in the build direction. Figure 10B shows the top of the build in which the top outer most edge contains a similar collection of grains.

Additional features are revealed through SEM imaging collected in Figure 11. First, in Figure 11A, a collection of larger grains appears in the central region of the structure along with differently oriented subgrains. These larger grains are elongated along the build direction and cross multiple build layers at once. At a higher magnification in Figure 11B, the sharp structures are shown to be cellular with walls measuring approximately 3 μm to 5 μm in width and 25 μm in length. Finally, as noted in Figure 11C, a transition occurs from columnar cells along the larger grains to a more evenly spaced cellular structure within the edge grains. An EDS line scan was done across these structures to identify the chemical composition. Scan results, seen in Figure 12, showed a consistent increase in the Hf concentration along the walls while the center of the structure remains Nb rich. SEM images of the BD – SD orientation, shown in Figure 13, reveal a zig – zag pattern that aligns with the back – and – forth scanning strategy used to build the sample. The large columnar grains, seen in Figure 13A, grow across multiple layers and contain a similar elongated structure, seen in Figure 13B.

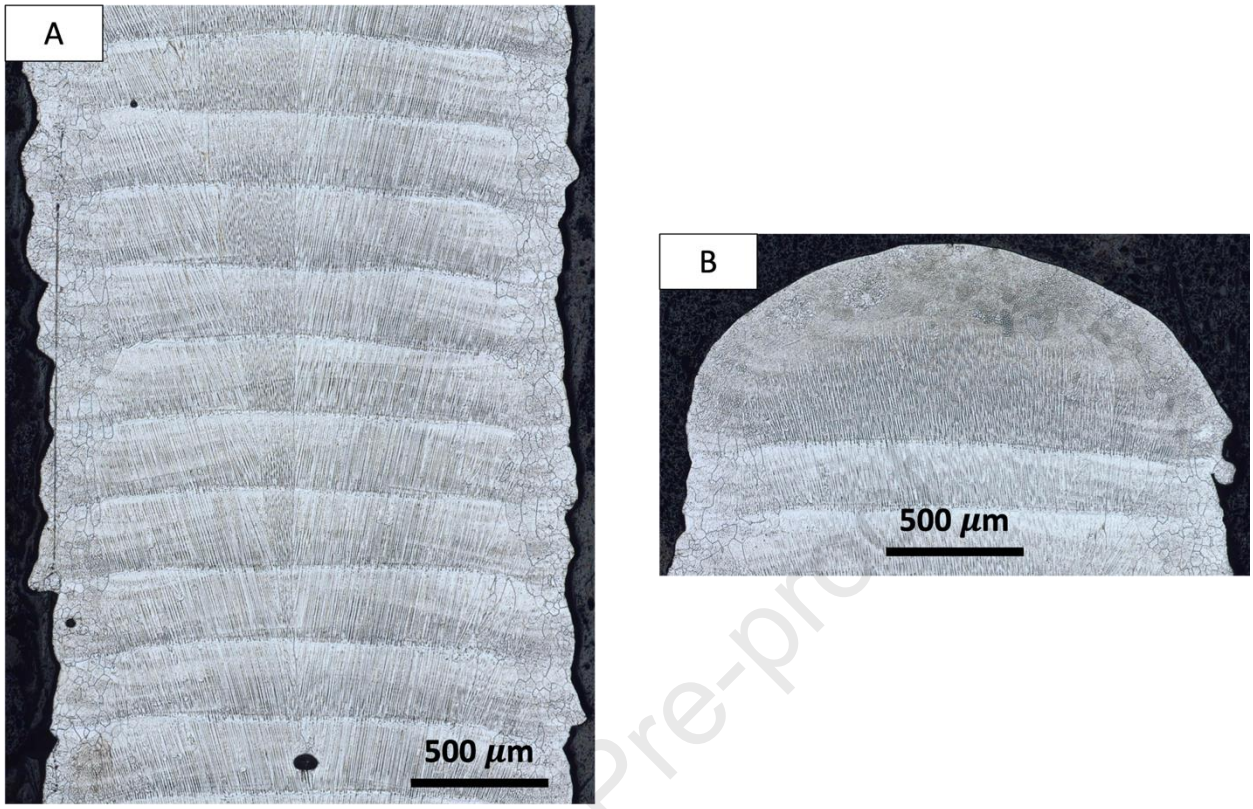

Fig. 10. Etched micrographs in the SR condition along the BD – TD direction. (a) Zoomed in section in the middle of the thin wall structure. Small grains are observed on the outer edges with a gradual transition to large epitaxial grains near the center. (b) Top layer of the thin wall structure showing small grains along the outer edge.

The difference in grain size and morphology, as well as the transition from columnar cells to evenly spaced ones can be explained by the thermal mechanisms common in the LP – DED process [60–64]. According to solidification theory, size and morphology of the grains are dictated by the temperature gradient *G* and the solidification growth rate *R* [65]. The morphology itself is driven by the ratio *G/R* while the size is governed by the cooling rate, defined as $G \times R$. As cooling rates are lowered, the grain sizes become larger, while increasing them leads to smaller grain sizes. While most metal systems are expected to have a mix of cellular and dendritic growth [65–67], higher *G/R* values favor more evenly spaced cellular structures, and a lower *G/R* value favors a more columnar cellular growth. An expansive review of the solidification process and grain growth direction in LP – DED is presented by Debroy et al. [30]. The presence of these cellular structures has been observed in previous work done by Liu et. al [68] when printing refractory high entropy alloy TiNbTaZrMo via L – PBF. Their work describes how these structures improve the mechanical properties of the material by hindering dislocation movement between cells.

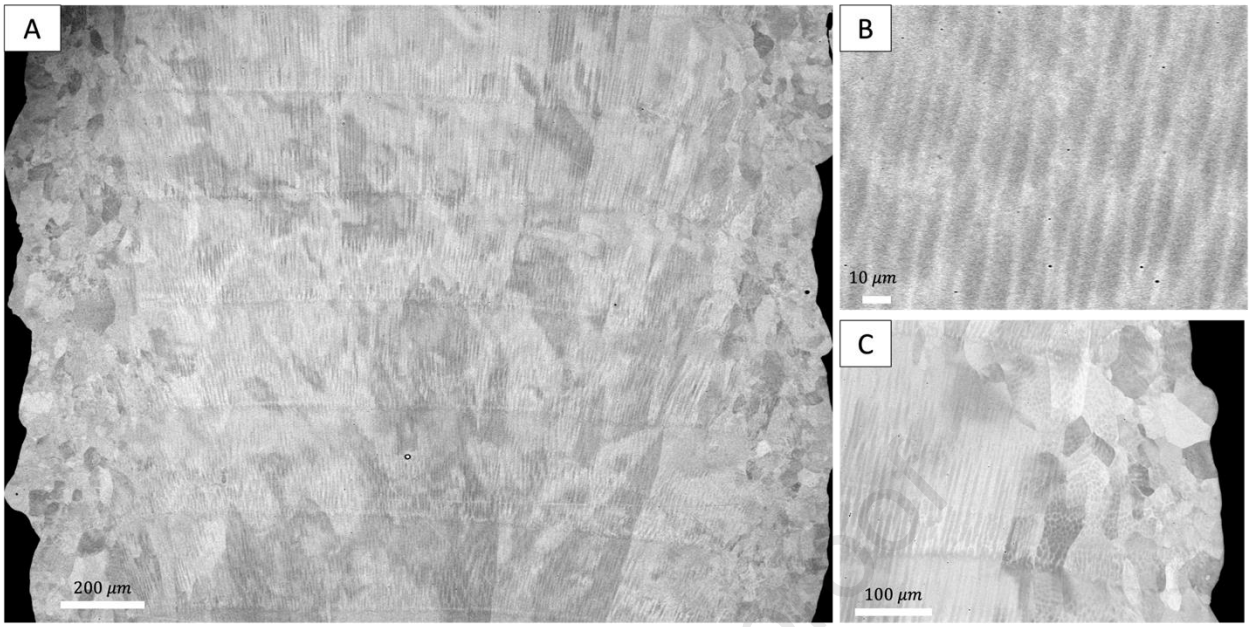

Fig. 11. SEM images of the etched SR samples in the BD – TD direction. (a) Overview of the sample at x65 magnification. (b) Epitaxial cellular structure spaced at 3 μm shown at x1000 magnification. (c) x250 magnification reveals transition between epitaxial cellular structure to an evenly spaced cellular structure in the small grains.

Values for *G* and *R* vary throughout the melt pool during the deposition process, making them difficult to calculate. Numerical simulations by Lee et. al [66] predicted increased cooling rates towards the edges of the melt pool which lead to smaller grain formation. Work by Nenadl et. al [67] showed similar morphologies where the bottom of the deposited layer showed planar growth, followed by columnar growth in the center and finally equiaxed grains at the top. Their work also showed how this effect applies to overlapping layers such as the case of LP – DED.

In the case of the microstructures presented in this work, the edges of the structure are exposed to the build chamber environment in which convection and radiation heat transfer aid the cooling process. This leads to an increase in the temperature difference and subsequently the temperature gradient, *G*. In turn, the cooling rate $G \times R$ and the *G/R* ratio are increased, resulting in a smaller grain size and a preference for a more even cellular structure. In the center of the 3D printed component, conduction is the predominant heat transfer mode, where the baseplate or the already deposited material acts as the main heat sink driving the direction of growth. This results in the opposite effect, where $G \times R$ and the *G/R* ratio are decreased, leading to larger grains and epitaxial columnar growth. This is further evidence by the microstructure in Figure 10B, where the top portion of the final layer shows smaller grains due to the faster cooling rates. The microstructure of the BD – SD view provides additional insights in this discussion. The grains along the edge of the BD – TD view align with the large columnar grains that follow the zig – zag pattern in the BD – SD view. This suggests that the edge grains are the cross section of the large columnar grains growing along the scan direction and therefore the varying grain sizes are due to changes in the grain growth direction.

Development efforts for C103 via L – PBF by Awasthi et. al [27] showed similar columnar grains along the build direction. Reported grain sizes are on the order of 56 μm, significantly smaller than the columnar grains observed in this work. L – PBF and EB – PBF work done by Phillips et al. [22] follow a similar trend for columnar grains that cross several build layers. Fabrication of pure Nb components by Martinez et. al [24] using EB – PBF also resulted in a columnar grain structure parallel to the build direction

and smaller grains on the top surface of the build. However, none of these studies reported smaller grains near the side edges of the structure nor did they report Hf rich cellular structures as observed in this work, indicating that these are unique features to the fabrication of C103 in the LP – DED process.

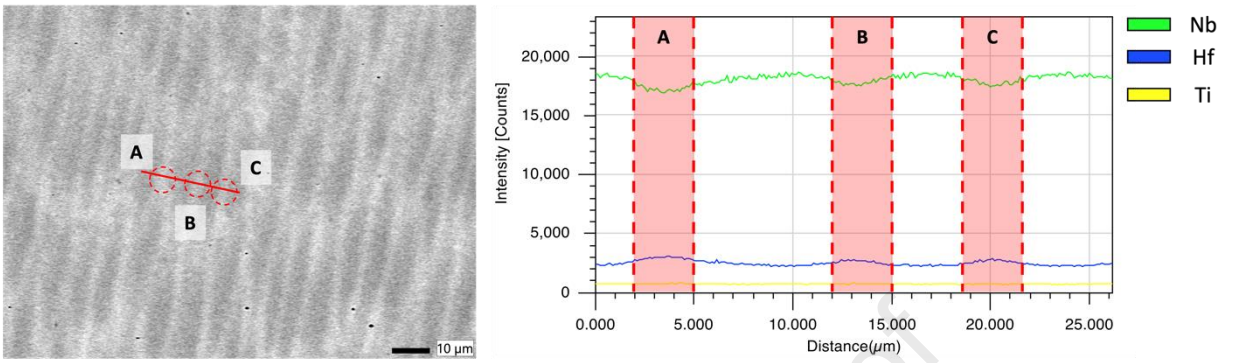

Fig. 12. EDS analysis of the cellular structure. Intensity counts of Nb, Hf, and Ti composition along the line scan show a decrease in Nb and an increase in Hf for each of the scanned walls of the cellular structure.

Studies for other alloy systems printed with LP – DED have shown comparable results to that observed in this study. For example, Zhang et. al show central epitaxial columns parallel to the build direction with smaller grains at the top of the final layer via SEM imaging of a nickel based superalloy printed with LP – DED [69]. EBSD analysis for single passes of 316L by Balit et. al [70] showed large epitaxial grain growth in the center and smaller grains throughout the edges of the bead. In this study epitaxial columnar growth is not reported. Microstructural characterization for Fe-Ni base alloy NASA HR – 1 by Chen et. al [71] reported a similar microstructure. However, in contrast to the findings presented in this work, the epitaxial cellular formation was angled towards the center of the thin wall structure and do not appear to nucleate from the bottom of the build layer. The observed zig – zag behavior can be attributed to the thermal history during the print process, in which crystal formation is influenced by the direction of the thermal gradient as observed by Demeneghi et. al and other studies [63,64,70,72]. Similar behaviors are also present in bulk feature geometries that were printed with a hatch and contour scanning strategy. While not presented in detail in this paper, several examples of this are discussed in [73–76] for a variety of alloy systems.

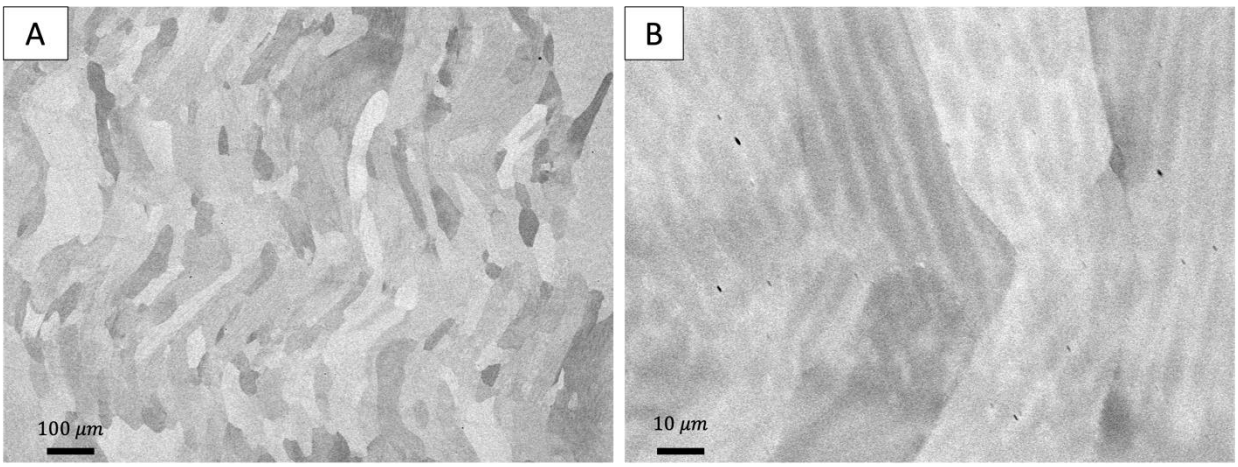

Fig. 13. SEM images of the BD – SD direction. (a) x100 magnification shows zig – zag structure across layer heights. (b) x1000 magnification reveals Hf cellular structure within the grains follows the zig – zag pattern.

EBSD was performed on the BD – TD, BD – SD and SD – TD faces for samples in the SR condition. Figure 14 shows the Inverse Pole Figures (IPFs) and their respective Pole Figures (PFs). Scans for the BD – TD direction reveal a sharp [001] texture for the large epitaxial grains in the center region while the smaller equiaxed grains along the edges have a more random texture. The sharp [001] texture is expected due to the fact that BCC metals, such as Nb, favor growth along the <001> direction as they solidify [77]. From the top view, given by the SD – TD scan, a similar pattern can be observed with the central region having a slightly more random texture. Finally, the front view given by the BD – SD scan, reveals that a large portion of the zig – zag grains have a [101] texture. The small grains observed in between layers could suggest remelting and quick solidification of the top portion of the previous layer.

Awasthi et. al [27] performed EBSD scans in the BD – TD face during their development work of C103 for L – PBF. The authors also observed a sharp [001] texture, parallel to the build direction. Comparable results have been reported by Mireles et. al [21] when evaluating the same orientation. A study on pure Nb printed via L – PBF by Griemsmann et. al [28] also revealed a zig – zag pattern when scanning the SD – TD face. Studies focused on LP – DED of other alloy systems have reported similar findings. For example, the results from Balit et. al on 316 L show the same zig – zag pattern but with a higher amount of small grains in between layers. Demeneghi et. al [64] evaluated GRCop-42 and observed the zig – zag structure but with a strong [001] texture and a lack of small grains in between alternating directions. Scans on the BD – TD and SD – TD faces revealed less defined orientations in the central regions and random texture along the edges. These previous results highlight that the work presented here reveal a unique combination of the sharp [001] texture, the zig – zag pattern, and collection of small grains in between that are unique to the manufacturing of C103 via the LP – DED process.

Using these same single scans, grain area percentages were determined. The grains have an average area of 784 μm^2. Approximately 64% of the total measured grains were smaller than or equal to 50 μm^2. The max grain size measured, corresponding to the center columnar like grains, was on the order of 1.11 mm^2. The spatial change in grain size of these thin wall components will result in non – uniform mechanical properties. To evaluate the impact of this on functional builds in the future, mechanical characterization must be performed on components in this condition as well as those without the presence of these smaller grains. To do so, the development and application of post processing techniques will be essential for this task. A proper heat treatment schedule that achieves recrystallization as well as surface finishing techniques that can remove the presence of these smaller edge grains must be considered.

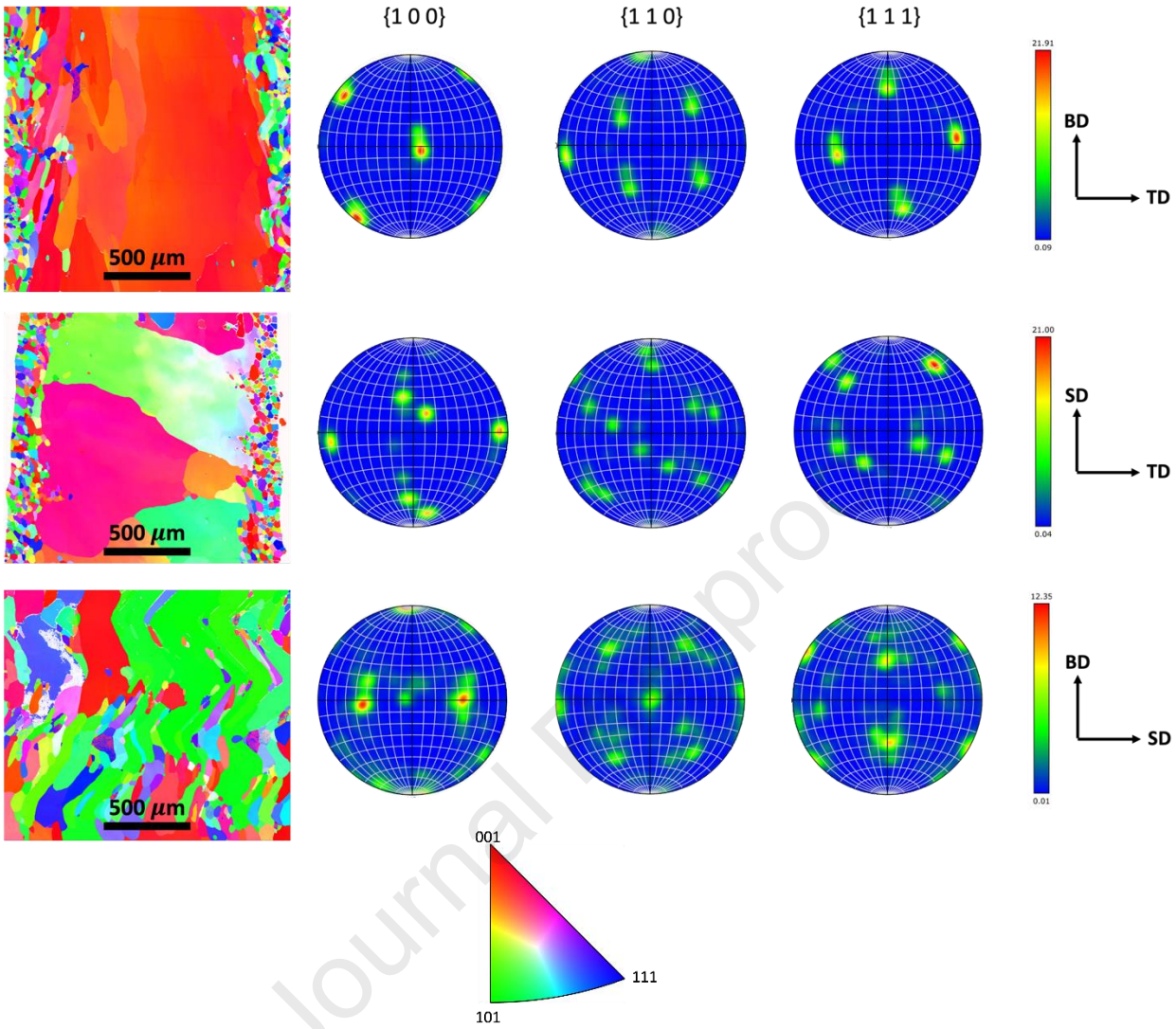

Fig. 14. IPF maps, from top to bottom, for BD – TD, SD – TD, and BD – SD directions and their respective Pole Figures (PF). The BD – TD exhibits a sharp [001] textured core. SD – TD shows a more randomly textured core as well as outer edges. BD – SD shows zig – zag pattern typical of LP – DED process due to the back – and – forth scanning strategy used.

3.5 Microhardness

Microhardness was characterized on the BD – TD face of the selected parameter set by performing Vickers Hardness (HV) testing. Measurements were taken on both the AB and SR conditions along the edge and center of the samples. The results are summarized by the Box and Whisker Plot in Figure 15 which graphically depicts the median, upper and lower quartiles, and upper and lower outliers of the corresponding hardness datasets [78,79].

The AB condition exhibits a relatively small difference in average between the edge and the center. The dataset exhibits a large spread in values as observed by the number of outliers present in both edge and center locations. Upon applying the SR cycle, the average hardness drops by up to 11.85% in the central region and the spread in the overall data is significantly reduced. The heat treatment cycle also

led to a more pronounced difference in the average values by up to 11% between the center and edge areas. These differences between the AB and SR conditions have been well documented by a variety of sources [80–83] and can be attributed to the elimination of dislocations. This difference can be indicative of a higher concentration of dislocations being present in the epitaxial columnar region in the as – built condition. Further characterization efforts are required for confirmation.

In general, the center of the structure exhibits lower hardness than the edge in both conditions, with differences of 2.7% in the AB condition and 9% in the SR. While these differences are relatively small, they can be attributed to the difference in grain size observed in the microstructure. The central region is characterized by the presence of larger grains and corresponds to the lower microhardness values. The edge of the sample intersects the zig – zag grains, leading to smaller cross sectional grain areas that result in increased microhardness values. This difference is explained by the Hall Petch effect, which states that smaller grains will have a higher strength by preventing more dislocation motion compared to larger grains [84,85].

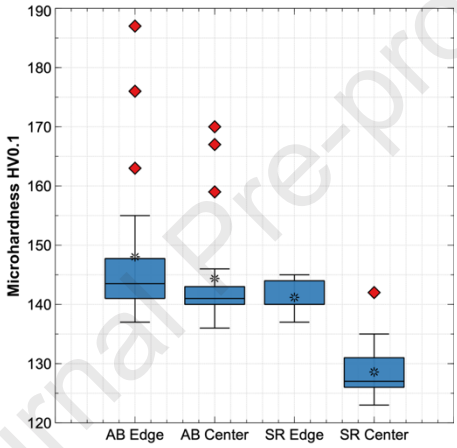

Fig. 15. Box and Whisker Plot of the collected microhardness measurements. The SR cycle reduces the spread of the data and leads to a wider difference in average values between the edge and center grains.

4 Summary and Conclusions

Laser powder – directed energy deposition (LP – DED) can overcome the size limitation of many other AM processes while still maintaining resolution levels of 1 mm. Many applications in aerospace and nuclear can leverage the use of refractory metals for high temperature environments that require structural integrity. The results presented in this article can help guide the development process for the adoption of LP – DED C103 by narrowing the process window. Results show viability and scalability for thin wall structures manufactured via LP – DED using C103 feedstock. Potential future work should characterize the mechanical properties at relevant operating environments such elevated temperature tensile testing and low cycle fatigue.

This study presents the parameter development process and the microstructural characterization of LP – DED C103. Optical micrographs, SEM images, and EBSD analysis were collected for the selected laser power and scanning speed combination. The conclusions are summarized as follows:

- Thin wall structures were successfully printed via LP – DED C103 resulting in relative densities greater than 99% and porosity below 0.09%. The high-density values are on par with results from

L – PBF and EB – PBF parts, indicating that fully dense C103 parts can be manufactured with this technology as well. A laser power and scanning speed of 1420 W and 14 mm/s respectively are recommended as starting point parameters for future development efforts.

- Evaluating the design of experiments parameters based on relative density alone, as is traditional of laser – powder bed fusion (L – PBF), is not sufficient for LP – DED. Several parameter sets that produced fully dense components also produced parts with inconsistent weld bead profiles. The recommendation from this study is to use geometrical accuracy in addition to relative density as the target parameters for LP – DED development efforts.
- A combination of optical microscopy and SEM revealed a large epitaxial growth in the central region with an elongated cellular structure and smaller grains along the edges with an evenly spaced cellular structure. A zig – zag pattern for grain growth is revealed in the BD – SD view of the samples. EDS scans revealed Hf rich walls in the cellular structure. The size, morphology, and transition from columnar cellular structures to evenly spaced ones appear to be unique to C103 printed with LP – DED.
- EBSD results show a strong [001] texture parallel to the build direction looking at the Build – Transverse direction. The front view, given by the Build – Scanning direction, revealed a zig – zag pattern following the back – and – forth deposition strategy that was used to build the samples. These patterns are consistent with results in literature regarding other metal systems manufactured with LP – DED.
- Microhardness measurements were taken for the AB and SR conditions along the central regions and the edges of the sample. The collected data exhibited a large amount of scatter which was reduced upon the application of the SR cycle, indicating that a large concentration of dislocations was present in the AB condition.

Declaration of Competing Interests

Lawrence E. Murr is an Associate Editor at the Journal of Materials Research and Technology. All other authors declare they have no known competing interests that may have influenced the presented work.

Acknowledgements

This work was performed at the W.M. Keck Center for 3D Innovation and was supported by NASA through Cooperative Agreement Notice (CAN) #80MSFC22N0001 and the NASA Space Technology Graduate Research Opportunity Fellowship (NSTGRO) Grant #80NSSC23K0107. Additional acknowledgments to the team at RPM Innovations for their support with troubleshooting during machine operation and insights to working with C103.

Author Contributions

BC – Conceptualization, Methodology, Writing – Original Draft, Data Collection, Formal Analysis; **KW** – Methodology, Supervision, Review & Editing; **TH** – Data Collection, Formal Analysis, Resources; **CR** – Data Collection, Formal Analysis, Resources; **OM** – Conceptualization, Supervision, **LM** – Review & Editing; **FM** – Funding Acquisition.

References

[1] T.W. Teasley, C.S. Protz, A.P. Larkey, B.B. Williams, P.R. Gradl, A Review Towards the Design Optimization of High Performance Additively Manufactured Rotating Detonation Rocket Engine Injectors, in: AIAA Propuls. Energy 2021 Forum, American Institute of Aeronautics and Astronautics, 2021. https://doi.org/10.2514/6.2021-3655.

[2] P.R. Gradl, S.E. Greene, C. Protz, B. Bullard, J. Buzzell, C. Garcia, J. Wood, R. Osborne, J. Hulka, K.G. Cooper, Additive Manufacturing of Liquid Rocket Engine Combustion Devices: A Summary of Process Developments and Hot-Fire Testing Results, in: 2018 Jt. Propuls. Conf., American Institute of Aeronautics and Astronautics, 2018. https://doi.org/10.2514/6.2018-4625.

[3] S. SOLLER, V. KAUFMANN, F. LAITHIER, Design and Testing of Liquid Propellant Injectors for Additive Manufacturing, (2017) 10 pages. https://doi.org/10.13009/EUCASS2017-306.

[4] B. Ridgeway, Hot-Fire Tests Show 3-D Printed Rocket Parts Rival Traditionally Manufactured Parts - NASA, (2013). https://www.nasa.gov/technology/manufacturing-materials-3-d-printing/hot-fire-tests-show-3-d-printed-rocket-parts-rival-traditionally-manufactured-parts/ (accessed October 17, 2023).

[5] V. Listek, Launcher Assembles Its First 3D Printed Spacecraft for Upcoming Mission - 3DPrint.com | The Voice of 3D Printing / Additive Manufacturing, 3DPrintCom Voice 3D Print. (2022). https://3dprint.com/292026/launcher-assembles-its-first-3d-printed-spacecraft-for-upcoming-mission/ (accessed October 17, 2023).

[6] A. Thryft, Lockheed & RedEye Team to 3D-Print Rocket Fuel Tanks, DesignNews (2016). https://www.designnews.com/design-hardware-software/lockheed-redeye-team-3d-print-rocket-fuel-tanks (accessed October 17, 2023).

[7] L. Mohon, NASA Additively Manufactured Rocket Engine Hardware Passes Cold Spray, Hot Fire Tests - NASA, (2021). https://www.nasa.gov/centers-and-facilities/marshall/nasa-additively-manufactured-rocket-engine-hardware-passes-cold-spray-hot-fire-tests/ (accessed October 17, 2023).

[8] C. Scott, Relativity Space 3D Prints 11-Foot-Tall Fuel Tank with Stargate 3D Printer, 3DPrintcom Voice 3D Print. Addit. Manuf. (2018). https://3dprint.com/231703/relativity-space-3d-prints-fuel-tank/ (accessed October 17, 2023).

[9] B. Ridgeway, Successful NASA Rocket Fuel Pump Tests Pave Way for 3-D Printed Demonstrator Engine - NASA, (2015). https://www.nasa.gov/technology/manufacturing-materials-3-d-printing/successful-nasa-rocket-fuel-pump-tests-pave-way-for-3-d-printed-demonstrator-engine/ (accessed October 17, 2023).

[10] 222XR Laser Deposition System, RPM Innov. (n.d.). https://www.rpm-innovations.com/laser-deposition-systems-222xr.html (accessed November 20, 2023).

[11] 557XR Laser Deposition System, RPM Innov. (n.d.). https://www.rpm-innovations.com/laser-deposition-systems-557xr.html (accessed November 20, 2023).

[12] Manufacturing Solutions, Formalloy (n.d.). https://www.formalloy.com/manufacturing-solutions (accessed November 20, 2023).

[13] O. Marketing, Metal 3D printing for prototype and for repair applications for small parts, Optomec (n.d.). https://optomec.com/3d-printed-metals/lens-printers/low-cost-metal-3d-printer/ (accessed November 20, 2023).

[14] S. Watson, LENS CS 600 System, Optomec (n.d.). https://optomec.com/lens-cs-600-system/ (accessed November 20, 2023).

[15] S. Watson, LENS CS 800 System, Optomec (n.d.). https://optomec.com/lens-cs-800-system/ (accessed November 20, 2023).

[16] O. Marketing, Large metal component part repair - LENS 850-R Systems, Optomec (n.d.). https://optomec.com/3d-printed-metals/lens-printers/metal-component-repair-3d-printer/ (accessed November 20, 2023).
[17] P. Hanaphy, Relativity Space unveils new fourth-gen Stargate 3D printer: technical specifications and pricing, 3D Print. Ind. (2022). https://3dprintingindustry.com/news/relativity-space-unveils-new-fourth-gen-stargate-3d-printer-technical-specifications-and-pricing-216149/ (accessed November 20, 2023).
[18] C.P. Garcia, S.W. Skinner, O.R. Mireles, P.R. Gradl, R. Osborne, J. Harris, Functional Design for Metal Additive Manufacturing, in: Met. Addit. Manuf. Propuls. Appl., American Institute of Aeronautics and Astronautics, Inc., 2022: pp. 439–526. https://doi.org/10.2514/5.9781624106279.0439.0526.
[19] T.C. Varney, T. Oldham, Md.I. Noor, P.F. Rottmann, Quantifying the Microstructure and Mechanical Property Differences between Bulk and Thin-wall Additively Manufactured Inconel 718, Materialia 31 (2023) 101867. https://doi.org/10.1016/j.mtla.2023.101867.
[20] J.A. Halchak, J.L. Cannon, C. Brown, Materials for Liquid Propulsion Systems, in: Aerosp. Mater. Appl., American Institute of Aeronautics and Astronautics, Inc., 2018: pp. 641–698. https://doi.org/10.2514/5.9781624104893.0641.0698.
[21] O. Mireles, O. Rodriguez, Y. Gao, N. Philips, Additive Manufacture of Refractory Alloy C103 for Propulsion Applications, in: AIAA Propuls. Energy 2020 Forum, American Institute of Aeronautics and Astronautics, VIRTUAL EVENT, 2020. https://doi.org/10.2514/6.2020-3500.
[22] N.R. Philips, M. Carl, N.J. Cunningham, New Opportunities in Refractory Alloys, Metall. Mater. Trans. A 51 (2020) 3299–3310. https://doi.org/10.1007/s11661-020-05803-3.
[23] Standard Specification for Niobium-Hafnium Alloy Bar and Wire, (n.d.).
[24] E. Martinez, L.E. Murr, J. Hernandez, X. Pan, K. Amato, P. Frigola, C. Terrazas, S. Gaytan, E. Rodriguez, F. Medina, R.B. Wicker, Microstructures of Niobium Components Fabricated by Electron Beam Melting, Metallogr. Microstruct. Anal. 2 (2013) 183–189. https://doi.org/10.1007/s13632-013-0073-9.
[25] C.A. Terrazas, J. Mireles, S.M. Gaytan, P.A. Morton, A. Hinojos, P. Frigola, R.B. Wicker, Fabrication and characterization of high-purity niobium using electron beam melting additive manufacturing technology, Int. J. Adv. Manuf. Technol. 84 (2016) 1115–1126. https://doi.org/10.1007/s00170-015-7767-x.
[26] M. Liu, J. Zhang, C. Chen, Z. Geng, Y. Wu, D. Li, T. Zhang, Y. Guo, Additive manufacturing of pure niobium by laser powder bed fusion: Microstructure, mechanical behavior and oxygen assisted embrittlement, Mater. Sci. Eng. A 866 (2023) 144691. https://doi.org/10.1016/j.msea.2023.144691.
[27] P.D. Awasthi, P. Agrawal, R.S. Haridas, R.S. Mishra, M.T. Stawovy, S. Ohm, A. Imandoust, Mechanical properties and microstructural characteristics of additively manufactured C103 niobium alloy, Mater. Sci. Eng. A 831 (2022) 142183. https://doi.org/10.1016/j.msea.2021.142183.
[28] T. Griemsmann, A. Abel, C. Hoff, J. Hermsdorf, M. Weinmann, S. Kaierle, Laser-based powder bed fusion of niobium with different build-up rates, Int. J. Adv. Manuf. Technol. 114 (2021) 305–317. https://doi.org/10.1007/s00170-021-06645-y.
[29] J. Hebda, W. Chang, Niobium alloys and high temperature applications, (n.d.) 17.
[30] T. DebRoy, H.L. Wei, J.S. Zuback, T. Mukherjee, J.W. Elmer, J.O. Milewski, A.M. Beese, A. Wilson-Heid, A. De, W. Zhang, Additive manufacturing of metallic components – Process, structure and properties, Prog. Mater. Sci. 92 (2018) 112–224. https://doi.org/10.1016/j.pmatsci.2017.10.001.
[31] A. Dass, A. Moridi, State of the Art in Directed Energy Deposition: From Additive Manufacturing to Materials Design, (2019) 26.
[32] D. Svetlizky, M. Das, B. Zheng, A.L. Vyatskikh, S. Bose, A. Bandyopadhyay, J.M. Schoenung, E.J. Lavernia, N. Eliaz, Directed energy deposition (DED) additive manufacturing: Physical

characteristics, defects, challenges and applications, Mater. Today 49 (2021) 271–295. https://doi.org/10.1016/j.mattod.2021.03.020.
[33] D.R. Feenstra, A. Molotnikov, N. Birbilis, Utilisation of artificial neural networks to rationalise processing windows in directed energy deposition applications, Mater. Des. 198 (2021) 109342. https://doi.org/10.1016/j.matdes.2020.109342.
[34] D.-G. Ahn, Directed Energy Deposition (DED) Process: State of the Art, Int. J. Precis. Eng. Manuf.-Green Technol. 8 (2021) 703–742. https://doi.org/10.1007/s40684-020-00302-7.
[35] D. Svetlizky, Directed energy deposition (DED) additive manufacturing: Physical characteristics, defects, challenges and applications, 49 (2021) 25.
[36] D. Svetlizky, B. Zheng, A. Vyatskikh, M. Das, S. Bose, A. Bandyopadhyay, J.M. Schoenung, E.J. Lavernia, N. Eliaz, Laser-based directed energy deposition (DED-LB) of advanced materials, Mater. Sci. Eng. A 840 (2022) 142967. https://doi.org/10.1016/j.msea.2022.142967.
[37] Latin Hypercube sampling — SMT 2.0b1 documentation, (n.d.). https://smt.readthedocs.io/en/latest/_src_docs/sampling_methods/lhs.html (accessed March 2, 2023).
[38] Y. Choi, D. Song, S. Yoon, J. Koo, Comparison of Factorial and Latin Hypercube Sampling Designs for Meta-Models of Building Heating and Cooling Loads, Energies 14 (2021) 512. https://doi.org/10.3390/en14020512.
[39] S. Dutta, A.H. Gandomi, Chapter 15 - Design of experiments for uncertainty quantification based on polynomial chaos expansion metamodels, in: P. Samui, D. Tien Bui, S. Chakraborty, R.C. Deo (Eds.), Handb. Probabilistic Models, Butterworth-Heinemann, 2020: pp. 369–381. https://doi.org/10.1016/B978-0-12-816514-0.00015-1.
[40] P. Saves, R. Lafage, N. Bartoli, Y. Diouane, J. Bussemaker, T. Lefebvre, J.T. Hwang, J. Morlier, J.R.R.A. Martins, SMT 2.0: A Surrogate Modeling Toolbox with a focus on hierarchical and mixed variables Gaussian processes, Adv. Eng. Softw. 188 (2024) 103571. https://doi.org/10.1016/j.advengsoft.2023.103571.
[41] Standard Test Method for Density of Powder Metallurgy (PM) Materials Containing Less Than Two Percent Porosity, (n.d.).
[42] Z. Wang, E. Denlinger, P. Michaleris, A.D. Stoica, D. Ma, A.M. Beese, Residual stress mapping in Inconel 625 fabricated through additive manufacturing: Method for neutron diffraction measurements to validate thermomechanical model predictions, Mater. Des. 113 (2017) 169–177. https://doi.org/10.1016/j.matdes.2016.10.003.
[43] D. Romanenko, V.J. Prakash, T. Kuhn, C. Moeller, W. Hintze, C. Emmelmann, Effect of DED process parameters on distortion and residual stress state of additively manufactured Ti-6Al-4V components during machining, Procedia CIRP 111 (2022) 271–276. https://doi.org/10.1016/j.procir.2022.08.020.
[44] F. Caiazzo, V. Alfieri, G. Bolelli, Residual stress in laser-based directed energy deposition of aluminum alloy 2024: simulation and validation, Int. J. Adv. Manuf. Technol. 118 (2022) 1197–1211. https://doi.org/10.1007/s00170-021-07988-2.
[45] A.L. Vyatskikh, X. Wang, J. Haley, B. Zheng, L. Valdevit, E.J. Lavernia, J.M. Schoenung, Residual stress mitigation in directed energy deposition, Mater. Sci. Eng. A 871 (2023) 144845. https://doi.org/10.1016/j.msea.2023.144845.
[46] J. Schneider, N. Shamsaei, S. Shao, R. Ghiaasiaan, S. Guo, P. McGill, T. Belcher, Microstructure and Properties of Additively Manufactured Metal Alloys, in: Met. Addit. Manuf. Propuls. Appl., American Institute of Aeronautics and Astronautics, Inc., 2022: pp. 237–306. https://doi.org/10.2514/5.9781624106279.0237.0306.
[47] ISO 6507-1:2023, Metallic Materials — Vickers Hardness Test — Part 1: Test Method, (n.d.). https://www.iso.org/obp/ui/#iso:std:iso:6507:-1:ed-5:v1:en (accessed November 20, 2023).

[48] S.R. Yarasi, A.R. Kitahara, E.A. Holm, A.D. Rollett, Powder Bed Fusion, in: E. Pei, A. Bernard, D. Gu, C. Klahn, M. Monzón, M. Petersen, T. Sun (Eds.), Springer Handb. Addit. Manuf., Springer International Publishing, Cham, 2023: pp. 389–405. https://doi.org/10.1007/978-3-031-20752-5_24.

[49] S. Wolff, Directed Energy Deposition, in: E. Pei, A. Bernard, D. Gu, C. Klahn, M. Monzón, M. Petersen, T. Sun (Eds.), Springer Handb. Addit. Manuf., Springer International Publishing, Cham, 2023: pp. 459–474. https://doi.org/10.1007/978-3-031-20752-5_28.

[50] P.R. Gradl, C.S. Protz, M. Le Corre, O.R. Mireles, F. Medina, M. Kottman, M. Norfolk, L. Ajdelsztajn, P. Allison, A. Elliott, Y. Bandari, Metal Additive Manufacturing Processes and Selection, in: Met. Addit. Manuf. Propuls. Appl., American Institute of Aeronautics and Astronautics, Inc., 2022: pp. 49–186. https://doi.org/10.2514/5.9781624106279.0049.0186.

[51] C. Kantzos, Feedstock for Metal Additive Manufacturing, in: Met. Addit. Manuf. Propuls. Appl., American Institute of Aeronautics and Astronautics, Inc., 2022: pp. 405–438. https://doi.org/10.2514/5.9781624106279.0405.0438.

[52] O. Mireles, W. Tilson, O. Rodriguez, J. Jones, D. Burkle, Characterizing Effects of Potential Build Induced Artifacts in L-PBF Components, in: AIAA Propuls. Energy 2020 Forum, American Institute of Aeronautics and Astronautics, 2020. https://doi.org/10.2514/6.2020-3507.

[53] S. Boslaugh, The Pearson Correlation Coefficient, in: Stat. Nutshell, 2nd ed., O'Reilly Media, Inc., n.d.: pp. 173–191. https://www.oreilly.com/library/view/statistics-in-a/9781449361129/ (accessed November 20, 2023).

[54] D.L. Hahs-Vaughn, Foundational methods: descriptive statistics: bivariate and multivariate data (correlations, associations), in: R.J. Tierney, F. Rizvi, K. Ercikan (Eds.), Int. Encycl. Educ. Fourth Ed., Elsevier, Oxford, 2023: pp. 734–750. https://doi.org/10.1016/B978-0-12-818630-5.10084-3.

[55] M. Kahlin, H. Ansell, J.J. Moverare, Fatigue behaviour of notched additive manufactured Ti6Al4V with as-built surfaces, Int. J. Fatigue 101 (2017) 51–60. https://doi.org/10.1016/j.ijfatigue.2017.04.009.

[56] J. Zhang, A. Fatemi, Surface roughness effect on multiaxial fatigue behavior of additive manufactured metals and its modeling, Theor. Appl. Fract. Mech. 103 (2019) 102260. https://doi.org/10.1016/j.tafmec.2019.102260.

[57] N. Sanaei, A. Fatemi, Analysis of the effect of surface roughness on fatigue performance of powder bed fusion additive manufactured metals, Theor. Appl. Fract. Mech. 108 (2020) 102638. https://doi.org/10.1016/j.tafmec.2020.102638.

[58] P. Gradl, A. Cervone, P. Colonna, Influence of build angles on thin-wall geometry and surface texture in laser powder directed energy deposition, Mater. Des. 234 (2023) 112352. https://doi.org/10.1016/j.matdes.2023.112352.

[59] M. Gharbi, P. Peyre, C. Gorny, M. Carin, S. Morville, P. Le Masson, D. Carron, R. Fabbro, Influence of various process conditions on surface finishes induced by the direct metal deposition laser technique on a Ti–6Al–4V alloy, J. Mater. Process. Technol. 213 (2013) 791–800. https://doi.org/10.1016/j.jmatprotec.2012.11.015.

[60] W.D. Callister Jr., D.G. Rethwisch, Dislocations and Strengthening Mechanisms, in: Mater. Sci. Eng. Introd., 10th ed., Wiley, n.d. https://www.wiley.com/en-us/Materials+Science+and+Engineering%3A+An+Introduction%2C+10th+Edition-p-9781119405498 (accessed November 22, 2023).

[61] A.C. Reardon, Heat Treatment of Nonferrous Alloys, in: Metall. Non-Metall. Second Ed., 2nd ed., ASM International, n.d. https://www.asminternational.org/books-and-handbooks/results/-/journal_content/56/10192/05306G/PUBLICATION/ (accessed November 22, 2023).

[62] A. Saboori, D. Gallo, S. Biamino, P. Fino, M. Lombardi, An Overview of Additive Manufacturing of Titanium Components by Directed Energy Deposition: Microstructure and Mechanical Properties, Appl. Sci. 7 (2017) 883. https://doi.org/10.3390/app7090883.
[63] C. Guévenoux, S. Hallais, A. Charles, E. Charkaluk, A. Constantinescu, Influence of interlayer dwell time on the microstructure of Inconel 718 Laser Cladded components, Opt. Laser Technol. 128 (2020) 106218. https://doi.org/10.1016/j.optlastec.2020.106218.
[64] G. Demeneghi, B. Barnes, P. Gradl, D. Ellis, J.R. Mayeur, K. Hazeli, Directed energy deposition GRCop-42 copper alloy: Characterization and size effects, Mater. Des. 222 (2022) 111035. https://doi.org/10.1016/j.matdes.2022.111035.
[65] S.A. David, S.S. Babu, J.M. Vitek, Welding: Solidification and microstructure, JOM 55 (2003) 14–20. https://doi.org/10.1007/s11837-003-0134-7.
[66] Y. Lee, M. Nordin, S.S. Babu, D.F. Farson, Effect of Fluid Convection on Dendrite Arm Spacing in Laser Deposition, Metall. Mater. Trans. B 45 (2014) 1520–1529. https://doi.org/10.1007/s11663-014-0054-7.
[67] O. Nenadl, V. Ocelík, J.Th.M. De Hosson, Texture development in direct powder deposition, J. Laser Appl. 29 (2017) 042007. https://doi.org/10.2351/1.5007944.
[68] C. Liu, Y. Wang, Y. Zhang, L.-C. Zhang, L. Wang, Deformation mechanisms of additively manufactured TiNbTaZrMo refractory high-entropy alloy: The role of cellular structure, Int. J. Plast. 173 (2024) 103884. https://doi.org/10.1016/j.ijplas.2024.103884.
[69] K. Zhang, W. Liu, X. Shang, Research on the processing experiments of laser metal deposition shaping, Opt. Laser Technol. 39 (2007) 549–557. https://doi.org/10.1016/j.optlastec.2005.10.009.
[70] Y. Balit, E. Charkaluk, A. Constantinescu, Digital image correlation for microstructural analysis of deformation pattern in additively manufactured 316L thin walls, Addit. Manuf. 31 (2020) 100862. https://doi.org/10.1016/j.addma.2019.100862.
[71] P.S. Chen, C.C. Katsarelis, W.M. Medders, P.R. Gradl, Segregation Evolution and Diffusion of Titanium in Directed Energy Deposited NASA HR-1, 2021. https://ntrs.nasa.gov/citations/20210013649 (accessed January 18, 2024).
[72] H.L. Wei, J. Mazumder, T. DebRoy, Evolution of solidification texture during additive manufacturing, Sci. Rep. 5 (2015) 16446. https://doi.org/10.1038/srep16446.
[73] A. Saboori, G. Piscopo, M. Lai, A. Salmi, S. Biamino, An investigation on the effect of deposition pattern on the microstructure, mechanical properties and residual stress of 316L produced by Directed Energy Deposition, Mater. Sci. Eng. A 780 (2020) 139179. https://doi.org/10.1016/j.msea.2020.139179.
[74] P.A. Kobryn, S.L. Semiatin, Microstructure and texture evolution during solidification processing of Ti–6Al–4V, J. Mater. Process. Technol. 135 (2003) 330–339. https://doi.org/10.1016/S0924-0136(02)00865-8.
[75] D.-K. Kim, W. Woo, E.-Y. Kim, S.-H. Choi, Microstructure and mechanical characteristics of multi-layered materials composed of 316L stainless steel and ferritic steel produced by direct energy deposition, J. Alloys Compd. 774 (2019) 896–907. https://doi.org/10.1016/j.jallcom.2018.09.390.
[76] D.R. Feenstra, V. Cruz, X. Gao, A. Molotnikov, N. Birbilis, Effect of build height on the properties of large format stainless steel 316L fabricated via directed energy deposition, Addit. Manuf. 34 (2020) 101205. https://doi.org/10.1016/j.addma.2020.101205.
[77] R.W. Fonda, D.J. Rowenhorst, Crystallographic Variability in Additive Manufacturing, IOP Conf. Ser. Mater. Sci. Eng. 1249 (2022) 012007. https://doi.org/10.1088/1757-899X/1249/1/012007.
[78] P. Costigan-Eaves, Edward R. *Tufte The visual display of quantitative information*, Inf. Des. J. 4 (1986) 235–236. https://doi.org/10.1075/idj.4.3.12cos.
[79] Y. Sun, M.G. Genton, Functional Boxplots, J. Comput. Graph. Stat. 20 (2011) 316–334. https://doi.org/10.1198/jcgs.2011.09224.

[80] J.L. Dossett, G.E. Totten, Steel Heat Treating Fundamentals and Processes, ASM International, 2013. https://doi.org/10.31399/asm.hb.v04a.9781627081658.

[81] M. Laleh, E. Sadeghi, R.I. Revilla, Q. Chao, N. Haghdadi, A.E. Hughes, W. Xu, I. De Graeve, M. Qian, I. Gibson, M.Y. Tan, Heat treatment for metal additive manufacturing, Prog. Mater. Sci. 133 (2023) 101051. https://doi.org/10.1016/j.pmatsci.2022.101051.

[82] H.D. Nguyen, A. Pramanik, A.K. Basak, Y. Dong, C. Prakash, S. Debnath, S. Shankar, I.S. Jawahir, S. Dixit, D. Buddhi, A critical review on additive manufacturing of Ti-6Al-4V alloy: microstructure and mechanical properties, J. Mater. Res. Technol. 18 (2022) 4641–4661. https://doi.org/10.1016/j.jmrt.2022.04.055.

[83] B.J. Mfusi, N.R. Mathe, L.C. Tshabalala, P.A. Popoola, The Effect of Stress Relief on the Mechanical and Fatigue Properties of Additively Manufactured AlSi10Mg Parts, Metals 9 (2019) 1216. https://doi.org/10.3390/met9111216.

[84] M. Gouné, É. Andrieu, Y. Bréchet, A. Deschamps, J. Douin, M. Fivel, A. Poulon-Quintin, 2 - The Basics to Better Understand Couplings in Physical Metallurgy, in: C. Blanc, I. Aubert (Eds.), Mech. - Microstruct. - Corros. Coupling, Elsevier, 2019: pp. 25–48. https://doi.org/10.1016/B978-1-78548-309-7.50002-8.

[85] Z.C. Cordero, B.E. Knight, C.A. Schuh, Six decades of the Hall–Petch effect – a survey of grain-size strengthening studies on pure metals, Int. Mater. Rev. 61 (2016) 495–512. https://doi.org/10.1080/09506608.2016.1191808.

Declaration of interests

☐ The authors declare that they have no known competing financial interests or personal relationships that could have appeared to influence the work reported in this paper.

☒ The authors declare the following financial interests/personal relationships which may be considered as potential competing interests:

Lawrence E. Murr is an Associate Editor at the Journal of Materials Research and Technology. If there are other authors, they declare that they have no known competing financial interests or personal relationships that could have appeared to influence the work reported in this paper.